RSC Advances

ROYAL SOCIETY OF CHEMISTRY

www.rsc.org/advances

Local structural evolution of $Fe_{54}C_{18}Cr_{16}Mo_{12}$ bulk metallic glass during tensile deformation and a temperature elevation process: A molecular dynamics study

Hui-Lung Chen,[1,a] Chia-Hao Su,[2,a] Shin-Pon Ju,[3,4,*] Shih-Hao Liu,[3]

and Hsin-Tsung Chen[5]

[1]Department of Chemistry and Institute of Applied Chemistry, Chinese Culture University, Taipei, 111, Taiwan

[2]Center for Translational Research in Biomedical Sciences, Kaohsiung Chang Gung Memorial Hospital, Kaohsiung 833, Taiwan

[3]Department of Mechanical and Electro-Mechanical Engineering, National Sun Yat-sen University, Kaohsiung 804, Taiwan

[4]Department of Medicinal and Applied Chemistry, Kaohsiung Medical University, Kaohsiung 807, Taiwan

[5] Department of Chemistry, Chung Yuan Christian University, Taoyuan City 32023, Taiwan

Corresponding Author:

* Shin-Pon Ju: jushin-pon@mail.nsysu.edu.tw

Telephone: +886-7-5252000 ext 4231

Fax: +886-7-5252000 ext 4201

Equally Contribution Note:

[a] Both authors contributed equally to this work

Abstract:

The mechanical and thermal properties of $Fe_{54}C_{18}Cr_{16}Mo_{12}$ bulk metallic glasses (BMGs) were investigated by the molecular dynamics simulation with the 2NN modified embedded-atom method (MEAM) potential. The fitting process of the cross-element parameters of 2NN MEAM (Fe-C, Fe-Cr, Fe-Mo, C-Cr, C-Mo, and Cr-Mo) was carried out first by the force matching method (FMM) on the basis of the reference data from the density functional theory (DFT) calculations. With these fitted parameters, the structure of $Fe_{54}C_{18}Cr_{16}Mo_{12}$ BMG was constructed by the simulated-annealing basin-hopping (SABH) method, and the angle distribution range of X-ray diffraction profile of the predicted $Fe_{54}C_{18}Cr_{16}Mo_{12}$ BMG closely matches that of the experiment profile, indicating the fitted 2NN MEAM parameters can accurately reflect the interatomic interactions of $Fe_{54}C_{18}Cr_{16}Mo_{12}$ BMG. The Honeycutt-Andersen (HA) index analysis results show a significant percentage of icosahedral-like structures within $Fe_{54}C_{18}Cr_{16}Mo_{12}$ BMG, which suggests an amorphous state. According to the tensile test results, the estimated Young's modulus of $Fe_{54}Cr_{16}Mo_{12}C_{18}$ bulk metallic glass is about 139 GPa and the large plastic region of the stress-strain curve shows that the $Fe_{54}C_{18}Cr_{16}Mo_{12}$ BMG possesses good ductility. Local strain distribution was used to analyze the deformation mechanism, and results show that a shear band develops homogeneously with the tensile fracture angle (θ_T) at about 50 degrees, in agreement with experimental results $45° < \theta_T < 90°$. For the temperature elevation results, the discontinuity of the enthalpy-temperature profile indicates the melting point $Fe_{54}Cr_{16}Mo_{12}C_{18}$ BMG is about 1310 K. The diffusion coefficients near the melting point were derived by the Einstein equation from the mean-square-displacement (MSD) profiles between 800-1400K. On the basis of diffusion coefficients at different temperatures, the diffusion barriers of

$Fe_{54}Cr_{16}Mo_{12}C_{18}$ can be determined by the Arrhenius equation. The diffusion barriers of total, Fe, Cr, Mo, C are 31.88, 24.68, 35.26, 22.50 and 31.79 KJ/mol, respectively. The diffusion barriers of Fe and Cr atoms are relatively lower, indicating Fe and Cr atoms more easily diffuse with the increasing temperature.

Keyword: Metallic glasses, Molecular dynamics simulation, mechanical properties, 2NN modified embedded-atom method (MEAM) potential, diffusion barrier

Introduction:

In 1960, Duwez [1] produced metallic glass using fast cooling rates, successfully fabricating an Au-Si system amorphous alloy. The formation of a non-crystalline structure is difficult, however, and in spite of the successful production of this amorphous alloy, there were size limitations. In early 1990, Inoue [2] proposed an empirical theory regarding the formation of an amorphous alloy that could more easily determine its composition and reduced the importance of cooling rates. As per Inoue's theory, forming an amorphous alloy requires three conditions: (1) a large negative heat, (2) three or more composition elements, and (3) the atomic size between elements must differ by more than 12%. In addition, Inoue also measured the thermal properties of amorphous alloys to investigate their glass-forming ability, and found that they require a crystallization temperature (T_x), glass transition temperature (T_g) and a supercooled liquid region (ΔT_x). With rising interest in amorphous alloys, studies found some elements that possessed high glass-forming ability, such as zirconium, palladium, iron, titanium, and copper. In addition, with advances in technology, the size of amorphous alloys became larger, which meant that bulk metallic glasses (BMG) could be produced. Diameters of bulk metallic glasses have been reported up to 2mm ~ 30mm [3, 4], which meant that amorphous alloys could be used in industry or other fields.

Bulk metallic glasses has become a potential material for applications due to their superior mechanical properties, such as high yielding strength up to 6 GPa [5,6], good ductility [7] and excellent corrosion resistance [8]. Accordingly, BMGs have attracted much attention, with some BMGs reported to be suitable for industrial or biomedical applications. For examples, it was reported that Zr-based BMGs present high biocompatibility with tests in NaCl and PBS (phosphate-buffered saline) solutions, showing good corrosion resistance to chloride (Cl) and phosphorus (P) ions [9-11]. Fe-based BMGs display a unique magnetic property, so it is often used in coil production [12-14]. In addition, Fe-based BMGs also have excellent corrosion resistance, allowing for their placement in the body as a biomedical implant material, of which 316L stainless steel, Ti-based BMG, and Co-Cr alloys are commonly used. Although those medical alloys are similar, studies have shown that 316L stainless steel is potentially harmful to the human body because its components contain nickel (Ni), which easily reacts to produce nickel ions after corroding. In recent years, some studies have indicated that the corrosion resistance of Fe-based BMG without nickel is greater than 316L stainless steel [15, 16]. In addition, Niinomi's [17] study reported that the Young's modulus of 316L stainless steel (180 GPa) is higher than human bone (about 10-30 GPa), resulting in a stress shielding effect which induces the atrophy of human bone, leading to the loosening of the implanted alloy and refracturing of the

human bone.

In 2010, Pilarczyk *et al.* successfully produced $Fe_{54}Cr_{16}Mo_{12}C_{18}$ BMG [18] and measured thermal properties such as glass transition temperature and crystallization temperature to investigate the glass forming ability of this BMG at different sizes. From these experimental results, $Fe_{54}Cr_{16}Mo_{12}C_{18}$ BMG shows a supercooled liquid temperature region arranging between 24 and 79 K, and this phenomena implies $Fe_{54}Cr_{16}Mo_{12}C_{18}$ BMG possesses a rather high glass forming ability and high thermal stability of the supercooled liquid. However, this study did not provide mechanical properties of $Fe_{54}Cr_{16}Mo_{12}C_{18}$, and no relevant studies have further reported them. Molecular dynamics simulation of mechanical properties of bulk metallic glass has shown a good degree of accuracy [19, 20]. In addition, it is very difficult to investigate the detailed local atomic arrangements around each compositional element and the variations of local atomic arrangements under external loading by the experimental approach directly. The possible alternative to investigate the local atomic arrangement of BMGs is by using numerical simulation. Among different numerical methods, molecular dynamics (MD) simulation can overcome the limitations of traditional empirical approaches and enable detailed observations on local structural variations and the deformation mechanism of BMGs under external loading on the atomic scale.

Therefore, this study will investigate mechanical and structural properties of $Fe_{54}Cr_{16}Mo_{12}C_{18}$ by molecular dynamics simulation. To the best of our knowledge, this study is the first to provide the interaction parameters between C and three other metal elements for this multi-element system by the force-matching method (FMM) [21]. By these potential parameters, the BMG model was constructed and the detailed local structural arrangements around each atom type were conducted. We also analyzed the changes in atomic structure under the tension test by HA pair analysis [22], and provided some explanations of the simulation results. In the future, we expect that this study can detail the design criterion of new materials for use in biomedical applications.

Simulation model:

In order to model the Fe-Cr-Mo-C alloy system by molecular dynamics (MD) simulation, the potential functions, employing the second-nearest neighbor modified embedded-atom method (2NN MEAM) [23, 24], were used to describe the interactions between different atomic pairs.

The 2NN MEAM potential form is shown as Eq. (1):

$$E = \sum_i [F_i(\overline{\rho}_i) + \frac{1}{2}\sum_{j(\neq i)} \phi_{ij}(R_{ij})] \quad (1)$$

where F is the embedding energy which is a function of the atomic electron density $\overline{\rho}_i$, and ϕ_{ij} is the pair potential interaction. The force-matching method (FMM) [25] was used to determine the 2NN MEAM parameters for Fe-C, Fe-Cr, Fe-Mo, Cr-C, Cr-Mo and Mo-C pairs. FMM is based on the variable optimization process of an objective function, and is constructed by the summation of squares of differences between the atomic forces obtained by a potential function and the corresponding atomic forces by *ab initio* or density functional theory (DFT) calculations. These parameters can be seen in the supplemental file.

After the parameters are fitted, they are used to generate the stable $Fe_{54}Cr_{16}Mo_{12}C_{18}$ amorphous structure by the simulation annealing basin-hopping (SABH) method [26] along the search direction for the energy local-minimal structure at higher energy. The unit cell with a total of 4000 atoms (2160 Fe, 640 Cr, 480 Mo and 720 C atoms) is shown in Fig. 1(a), and the model shown in Fig. 1(b) for the tension test by MD was constructed by replicating the unit cell to 6×3×6 for the x, y and z axes.

Next, the MD simulation was performed by the large-scale atomic/molecular massively parallel simulator (LAMMPS) developed by Plimpton and co-workers [27]. By MD simulation, the model was quenched from 1000 K to 300 K for 10 ps to relax the system with an NPT ensemble at 0 GPa. During the tensile process, the periodic boundary conditions (PBC) were applied to the x-, and y-dimensions and the open boundary was used in the z-dimension. The strain rates of 5×10^8 m/s were examined to obtain the appropriate strain rate for the current system. During the tension process, the tensile stress at different strains was calculated by the following equation in LAMMPS code [28]:

$$\sigma_{mn}=\frac{\sum_i -1\times\left[mv_i^m v_i^n+\frac{1}{2}\sum_{n=1}^{N_p}(r_{1m}F_{1n}+r_{2m}F_{2n})+\frac{1}{3}\sum_{n=1}^{N_a}(r_{1m}F_{1n}+r_{2m}F_{2n}+r_{3m}F_{3n})\right]}{\sum_i V_i} \quad (2)$$

where $\sum_{n=1}^{N_p}(r_{1m}F_{1n}+r_{2m}F_{2n})$ is the effect of the pairwise potential function and indexes 1 and 2 indicate two atoms interacting with each other. The term $\sum_{n=1}^{N_a}(r_{1m}F_{1n}+r_{2m}F_{2n}+r_{3m}F_{3n})$ is the effect of bond angle of the three atoms involved in the interaction. Indexes of m and n represent the m plane and n-direction. The r is the interatomic distance between two atoms 1 and j, m is the weight of the atom, and V_i is a local volume defined by:

$$V_i = \frac{2\pi \sum r_{ij}^{-1}}{3\sum r_{ij}^{-2}} \quad (3)$$

Results and Discussion

The $Fe_{54}C_{18}Cr_{16}Mo_{12}$ BMG unit cell of 4000 atoms obtained by SABH method was characterized by the X-ray diffraction (XRD) module REFLEX [29-31] in Accelrys Materials Studio 7.0 [32]. In REFLEX, Bragg's law is used to obtain the constructive interference intensity for X-rays scattered by materials, and its formula is listed as follows:

$$d = \frac{n\lambda}{2\sin\theta} \quad (4)$$

where θ is a certain angle of incidence when the cleavage faces of crystals appear to reflect X-ray beams. The term d is the distance between atomic layers in a crystal, and λ is the wavelength of the incident X-ray beam. When n is an integer, the diffraction is constructive with higher intensity. While n is a half integer, the diffraction is destructive and the intensity approaches zero.

The XRD and radial distribution function (RDF) profiles of $Fe_{54}C_{18}Cr_{16}Mo_{12}$ BMG are shown in Figs. 2(a) and 2(b). One can see no specific crystalline peak appearing in the 2θ range between 20° – 100° for the XRD profile, and the range of the XRD peak is located at 40°-60° and maximum intensity is around 50°, which is consistent with the previous experimental XRD profile of $Fe_{54}C_{18}Cr_{16}Mo_{12}$ BMG [18]. This indicates our model is in the amorphous state and the fitted cross-element potential parameters of 2NN MEAM can accurately predict the atomic arrangement of $Fe_{54}C_{18}Cr_{16}Mo_{12}$ BMG as used in the related experiments. For the RDF profile, the broad splitting second peak between 3 and 5 Å indicates the amorphous configuration of $Fe_{54}C_{18}Cr_{16}Mo_{12}$, which is consistent with the inference of the short range order by the XRD profile. According to the XRD and RDF profiles shown in Figs. 2(a) and 2(b), the $Fe_{54}C_{18}Cr_{16}Mo_{12}$ structure constructed by SABH is amorphous and corresponds to realistic $Fe_{54}C_{18}Cr_{16}Mo_{12}$ BMG in experiment.

A further study into the local microstructural distribution for $Fe_{54}C_{18}Cr_{16}Mo_{12}$ BMG was conducted by using the Honeycutt-Anderson (HA) pair analysis. The detailed definition of the HA index can be found elsewhere [33-35] and is not presented here. The HA indexes of 1421 and 1422 represent F.C.C. and H.C.P. crystal structures, and 1431, 1541, and 1551 which occupy the largest fraction in the amorphous or liquid state, are used to search the icosahedral local structures. The 1551 pair is particularly characteristic of the icosahedral ordering; the 1541 and 1431 are indexes for the defect icosahedra and F.C.C. defect local (or distorted icosahedra)

structures, respectively. HA indexes 1661 and 1441 are employed to identify the local B.C.C. structure. Finally, the indexes 1321 and 1311 are the packing related to rhombohedral pairs which tend to evolve when the 1551 packing forms, which can be viewed as a side product accompanying icosahedral atomic packing. The schematic diagrams for the HA indexes introduced above are illustrated in Fig. 3(a).

Figure 3(b) shows the HA index distribution of $Fe_{54}C_{18}Cr_{16}Mo_{12}$ BMG, and the fraction of icosahedra-like local structures (1551, 1541, and 1431) are about 47.7%. The fraction of the distorted icosahedral structure (1431) occupies the highest fraction of 21.6% among three icosahedra-like fractions, whereas the fraction of perfect icosahedral local structure (1551) is the lowest, with the occupancy of 11.2%. For other HA indexes, the B.C.C local structures (1441 and 1661), H.C.P local structure (1422), rhombohedral local structures (1321 and 1311), and F.C.C. local structure (1421) are about 12.1%, 6.9%, 25.3%, and 8.1%, respectively. The high HA fractions of icosahedra-like structures verify the amorphous $Fe_{54}C_{18}Cr_{16}Mo_{12}$ structure and are consistent with the HA analysis results reported previously for BMGs. Because the second index of the HA analysis is the number of common neighbor atoms between the investigated atomic pair, the higher fractions of 1321 and 1311 HA indexes indicate the local structures of a BMG are more open-packed [36]. Compared with the HA analysis of BMGs shown in previous studies [35, 37], the $Fe_{54}C_{18}Cr_{16}Mo_{12}$ BMG possesses relatively lower icosahedral-like HA fractions and relatively higher rhombohedral HA fractions, indicating more loose local structures distribute within the $Fe_{54}C_{18}Cr_{16}Mo_{12}$ BMG.

Since the atomic radii of Fe, C, Cr, and Mo are 1.40, 0.70, 1.40, and 1.45 Å, with the atomic size of C smaller than the other three by about 50.0%-51.7%, the HA fraction distributions for different atom type pairs are very different. Because the HA index profiles shown in Fig. 3(b) do not contain enough information about the HA fraction distributions for different atom pairs, they should be analyzed to better understand the local structural arrangements around different atom pairs with different pair lengths. Therefore, a more detailed analysis of the HA indexes of different atomic pairs in $Fe_{54}C_{18}Cr_{16}Mo_{12}$ BMG are shown in Fig. 4. Because Fe occupies the highest atomic fraction in $Fe_{54}C_{18}Cr_{16}Mo_{12}$ BMG, the Fe-related HA indexes (Fe-Fe, Fe-C, Fe-Cr, and Fe-Mo) are relatively higher than those for other atom type pairs, which can be seen in the first four fractions of each HA index of Fig. 4. The summations of the icosahedra-like HA indexes 1551, 1541, and 1431, referring to the liquid local structures, are about 23.02%, 13.14%, 7.81% and 8.06% for the atom pairs of Fe-Fe, Fe-C, Fe-Cr, and Fe-Mo, respectively. Although the element fraction of Fe is the highest in $Fe_{54}C_{18}Cr_{16}Mo_{12}$ BMG, one can see the icosahedra-like HA fractions of Fe-Fe and Fe-C are comparable. For the rhombohedral HA fractions, the Fe-Fe pair

forms the highest fractions of 1321 and 1311 among all pair types.

Table I lists the average coordination numbers (CNs) of Fe, C, Cr, and Mo atoms in $Fe_{54}C_{18}Cr_{16}Mo_{12}$ BMG as well as the partial coordination numbers of different atomic pairs. The coordinate number was calculated by counting the amount of first neighbor atoms around the center atom. The cutoff length for the CN calculation was estimated from the first minimal distance of the RDF profile as shown in Fig. 2(b). The first subscript for atomic pair indicates the type of the reference atom and the second subscript stands for the atom type of the first neighbor of the reference atom. Among the average CNs of these four elements, the Cr and Fe atoms have the highest and lowest CNs of 12.48 and 11.70, respectively. A closer investigation of the partial CNs of Fe-Fe, Cr-Fe, Mo-Fe, and C-Fe shows that the partial CN of Cr-Fe is the highest and that of Fe-Fe is the lowest.

The Warren-Cowley chemical short-range-order (CSRO) analysis [38] for $Fe_{54}C_{18}Cr_{16}Mo_{12}$ BMG was employed to quantify the attraction and repulsion between element pairs. With the CN information shown in Table 1, the chemical affinities of a referenced atom with its first neighbor atoms are evaluated by the CSRO parameter. The definition of this parameter is as the following equation:

$$\alpha_{ij} = 1 - \frac{N_{ij}}{c_j N_i} \tag{5}$$

where $\boldsymbol{\alpha}_{ij}$ is the CSRO parameter of the *i*-type referenced atom relative to *j*-type atom, N_{ij} is the partial CN for the *i*-type referenced atom relative to *j*-type atom, and c_j and N_i are the fractions of *j*-type atom within the alloy and the average CN of *i*-type atoms, respectively. The value of c_j by N_i is an ideal partial CN for the referenced *i*-type atom relative to the first neighbor *j*-type atom, and this value completely depends on the respective atomic composition fraction of $Fe_{54}C_{18}Cr_{16}Mo_{12}$. According to this analysis, it can be seen that if the alloys are in the ideal solution, the value of N_{ij} should be very close to c_jN_i and allows the value of α_{ij} to be 0. On the other hand, a value larger than 0 means the *j*-type atoms are less prone to gather around *i*-type atoms, causing the value of N_{ij} to be less than the number of ideal N_{ij}. For the same reason, a negative value means the *j*-type atoms are prone to gather around *i*-type atoms.

The CSRO parameters of all pairs of $Fe_{54}C_{18}Cr_{16}Mo_{12}$ BMG are listed in Table II. The results show that the CSRO parameters for Fe-Fe, Cr-Cr, and Mo-Mo are positive and that of C-C is relatively close to zero. This CSRO analysis result indicates the C atom has no preference to another C atom, and the three other elements display less affinity to themselves, indicating that this alloy easily forms the glass-like structure. Furthermore, most CSRO parameters of C-related pairs are negative except for C-Fe,

indicating that the affinities between C and the three other metal elements are relatively higher than Fe-related, Cr-related, and Mo-related ones, which reveals that the smallest atom, C, tends to pair with a metal atom instead of itself.

Figure 5 shows the stress-strain profile and ΔV/V value with strain for the $Fe_{54}C_{18}Cr_{16}Mo_{12}$ BMG under tension. One can see the stress increases linearly with strain while strain increases from 0 to 0.05, indicating the elastic behavior of $Fe_{54}C_{18}Cr_{16}Mo_{12}$ BMG is located within this strain range. The Young's modulus derived from the slope of the stress-strain profile between strains of 0 and 0.02 is about 139 GPa. At strains from 0.05 to 0.1, the stress displays a parabolic increase with increasing strain, and reaches its maximum value at about 6.83 GPa. At strains from 0.1 to 0.5, the stress shows the gradual decrease from its maximal value, indicating the occurrence of fracture. The stress-strain profile for $Fe_{54}C_{18}Cr_{16}Mo_{12}$ also shows a large plastic region, which can exceed 40%. This result is consistent with those shown in the recent related Fe-based studies [39, 40].

The ΔV/V value, the ratio of open volume (ΔV) to the system volume at strain 0 (V), was used to indicate the volume variation during the tension process. It is a generally held view that more open volume allows for more plastic deformation [41]. The system volume is defined as the summation of the atomic volume calculated by Eq. (6), and the ΔV value is calculated by the following equation:

$$\Delta V = V_{\varepsilon} - V_0 \quad (6)$$

where V_{ε} and V_0 are the system volumes at strains of ε and 0, respectively. Consequently, the ΔV/V value indicates the percentage increase in system volume during the tension. In Fig. 5, it is apparent that ΔV/V is linearly proportional to the strain within the elastic region from strain 0 to 0.05. At strains from 0.05 to 0.1, the open volume increases parabolically with the strain, and the linear increase of ΔV/V with the strain becomes more significant when the strain exceeds 0.1.

The atomic local shear strain η_i^{Mises} of an individual atom, introduced by Shimizu *et al.* [42], was used to monitor the development of shear transition zones (STZ) and the formation of the shear band within $Fe_{54}C_{18}Cr_{16}Mo_{12}$. The detailed definition of η_i^{Mises} can be found in reference [43] of this study and is therefore not introduced here. A large η_i^{Mises} value indicates atom *i* is under local plastic and shear deformation, whereas a small η_i^{Mises} value implies atom *i* undergoes a small amount of movement relative to all its first neighbor atoms or atom *i* is under local elastic deformation.

Figure 6(a)-(f) shows the snapshots of $Fe_{54}C_{18}Cr_{16}Mo_{12}$ BMG with atomic η_i^{Mises} values at strains of 0, 0.1, 0.2, 0.3, 0.4 and 0.5, which are labelled as letters **a-f** on the stress-strain curve of Fig. 5. For the reference structure at strain of 0, the η_i^{Mises} value of each atom is 0, and the initialization of STZs labeled with black dashed circles in Fig.6(b) occurs at strain of 0.1. These STZs distribute randomly within

$Fe_{54}C_{18}Cr_{16}Mo_{12}$ BMG. From Fig. 5, one can infer that the sufficient open volume increase significantly activates the initialization of shear banding and enhances the appearance of STZs when the strain exceeds the yielding strain. At strain of 0.2, the extension of STZs begins to form several shear bands, as indicted by the black dashed lines shown in Fig. 6(c), and more shear bands can be seen in Fig. 6(d) at strains of 0.3. In Fig. 5, the $\Delta V/V$ value increases more significantly with the strain when strain exceeds 0.1. From the η_i^{Mises} distributions shown in Figs. 6(c) and 6(d), one can note that the increase in the shear band number results in the significant increase of the open volume and a local structure rearrangement. The shear bands propagate at a direction 50^0 from the tensile direction and intersect with one another, resulting in the vein-like pattern. This vein-like pattern can be also seen in previous theoretical [44] and experimental studies [45,46]. These results show that good ductility of $Fe_{54}C_{18}Cr_{16}Mo_{12}$ might be caused by the homogeneous development of shear bands which increase the deformation area. Figure 6(e) and (f) shows the fracture areas at strains of 0.4 and 0.5, where considerable atomic rearrangements occur.

To understand the local structural rearrangement during the tension process, the numbers of different HA pairs for $Fe_{54}C_{18}Cr_{16}Mo_{12}$ BMG at different strains during the tension are illustrated in Fig. 7. The vertical axis represents the total number of one particular HA pair and the horizontal axis is the tensile strain. The reason that this study uses the number of pairs instead of pair fraction is that total bonding pairs at each strain will decrease due to increasing distance between atoms during the tensile process such that the fraction is not the best choice to represent the variation of local structure. It can be seen from Fig. 7 that the rhombohedral HA local structure 1311 is predominant at strain higher than 0.05. Among all HA pairs, there are three indexes with notable changes within the strain range 0 to 0.2. The 1551 and 1541 HA indexes, referring to the icosahedral and defected icosahedral structures, show considerable decreases such that the pair numbers of 244,523 and 351,527 for 1551 and 1541 at the beginning of the tensile test decrease to 209,597 and 314,310 at strain of 0.5. For 1311, this HA index increases with the strain from 553,386 to 628,940. Since the second index of the HA analysis is the number of common neighbor atoms between the investigated atomic pair, the decrease of HA indexes with the larger second indexes implies the local structures in $Fe_{54}C_{18}Cr_{16}Mo_{12}$ BMG become less dense during the tensile process. Note that because the third digit of the HA index represents the bonded number between the first neighbor atoms around the root HA pair, a lower third digit in the HA index indicates a less dense local structure if the first two HA index digits are the same. For example, 1541 is more loose than 1551. Consequently, the 1311 HA index indicates a relatively loose local structure when compared to that of the 1321 HA index. In Fig. 7, the reduced 1551 and 1541 local structures mostly

transform into 1311 structures, which is the most loose local structure among those indicated by the HA indexes.

The thermal behaviors of $Fe_{54}Cr_{16}Mo_{12}C_{18}$ were investigated by the MD temperature elevation process, starting from an initial temperature of 300 to 2000K. During this process, the TtN method [47], combining the Nose-Hoover thermostat with the Parrinello-Rahman variable shape size ensemble, was applied to the model shown in Fig. 1(a) with periodic boundary conditions in the x, y, and z dimensions. The TtN method was adopted to maintain a constant temperature and a constant stress of 0 during the temperature elevation simulation. The heating process was conducted by applying a temperature increment of 10 K to the system, which follows a relaxation process of 10 ps before applying the next temperature increment.

Figure 8 shows the enthalpy profile at different temperatures for $Fe_{54}C_{18}Cr_{16}Mo_{12}$ BMG during the heating process. The enthalpy value was calculated by taking the average of the enthalpy values of the immediately preceding 3 ps during the relaxation process. The enthalpy is determined from the following equation:

$$H = U + pV \tag{7}$$

where U is system energy; p is pressure, and V is the system volume.

In Fig. 8, the enthalpy is linearly proportional to the increasing temperature from 300 to 1310 K and the discontinuity of this profile appears at 1310 K. When the system temperature is higher than 1310K, the enthalpy is also linearly proportional to the increasing temperature. Consequently, the melting point (T_m) of $Fe_{54}C_{18}Cr_{16}Mo_{12}$ BMG is around 1310 K, at which the local structures begin to significantly change, leading to the discontinuity of the enthalpy profile at 1310 K.

The mean-square displacement (MSD) profiles at temperatures ranging from 800 to 1400 K for $Fe_{54}C_{18}Cr_{16}Mo_{12}$ were used to investigate their dynamical properties. The MSD is defined by a function of time as shown in Eq. (8):

$$MSD = \frac{\sum_i^N [r_i(t) - r_i(t_0)]^2}{N} \tag{8}$$

where $r_i(t)$ represents the position of atom i at delay time t, and $r_i(t_0)$ indicates the reference position of the corresponding atom at reference time t_0; N represents the total atom number of the investigated system. From Fig. 9, it is clear that the slopes of the MSD profile are generally larger with the increasing temperature.

It is known that the MSD profile is linear to the delay time over the long-time limit, and thus the diffusion coefficients of $Fe_{54}C_{18}Cr_{16}Mo_{12}$ can be derived from the slopes of MSD profiles after a longer delay time by the Einstein equation [48]:

$$D = \frac{1}{6N}\lim_{t\to\infty}\frac{d}{dt}MSD \quad (9)$$

where D is the self-diffusion coefficient and N is the number of atoms. The MSD profiles of different elements at different temperatures derived from the Einstein equation for the Fe, C, Cr, and Mo diffusion coefficients of $Fe_{54}C_{18}Cr_{16}Mo_{12}$ BMG at different temperatures.

In Roy's study, they used the Arrhenius equation to derive the diffusion barrier of Zr and Si atoms on the basis of the calculated diffusion coefficient near the melting points of crystal $ZrSi_2$ [49]. The formula of the Arrhenius equation for describing the diffusion coefficient at different temperatures is:

$$D = D_0 \times e^{(\frac{-Q}{RT})} \quad (10)$$

where Q is the activation energy, T is the temperature, D_0 is the pre-exponential factor, and R is the Boltzmann constant. To calculate the diffusion barrier, the profiles of ln(D) versus 1/T for total, Fe, Cr, Mo and C atoms are shown in Fig. 10. It can be inferred that the diffusion coefficients of $Fe_{54}C_{18}Cr_{16}Mo_{12}$ significantly increase with increasing temperature. Note that the ln(D) profile is proportional to the inverse of the temperature, and the diffusion barriers of total, Fe, Cr, Mo and C atoms can be derived by the slopes of the ln(D) profiles. The D_o values and the diffusion barriers are listed in Table III. The diffusion barriers of total, Fe, Cr, Mo, C are 31.88, 24.68, 35.26, 22.50 and 31.79 KJ/mol, respectively. For Fe and Cr atoms, the diffusion barriers are relatively lower, indicating that Fe and Cr atoms more easily diffuse with increasing temperature.

Conclusion:

Molecular dynamics simulations have been conducted to investigate the mechanical properties and thermal properties of $Fe_{54}C_{18}Cr_{16}Mo_{12}$ BMG by tension and temperature elevation processes, respectively. The unit cell of $Fe_{54}C_{18}Cr_{16}Mo_{12}$ BMG built by the SABH method is examined by XRD analysis and the XRD profile closely matches that of experimental $Fe_{54}C_{18}Cr_{16}Mo_{12}$ BMG, indicating $Fe_{54}C_{18}Cr_{16}Mo_{12}$ BMG from our SABH prediction is totally amorphous and the atomic arrangement of our model is very similar to those used in the experiment. From the HA index analyses, the icosahedra-like structures that indicate liquid local structures appear to be the major local structures in the $Fe_{54}C_{18}Cr_{16}Mo_{12}$ BMG. The considerable icosahedra-like structures improve the glass forming ability by forming denser and more stable local clusters. Furthermore, chemical affinities are investigated by CSRO parameters. The C-related pairs are nearly all negative except for C-Fe and are relatively higher than Fe-related, Cr-related, and Mo-related pairs,

which indicate that the C atom tends to pair with a metal atom instead of itself. This demonstrates that a high diversity of atom size in the solution will advance the formation of the amorphous state.

Based on the stress-strain profile obtained from the tensile test, the predicted Young's modulus is about 139 GPa, which is much less than conventional biomedical implants, such as 316L stainless steel and Co-Cr alloy. In addition, the HA pair analysis of variation in the open volume is also employed to monitor the development of STZ [50] and the evolution of the shear band. The distributions of the stress-strain curve and open volume with strain show linear increases of stress-strain and open volume-strain curves, which suggest an elastic region. Moreover, stress and open volume increase significantly at STZ initialization stages when the strain exceeds 0.1. This can be attributed to an increase in the number of shear bands, resulting in a significant increase of open volume and the activation of local structural rearrangement. In addition, shear bands measured by the local atomic strain develop along a direction 50^0 from the tensile direction and indicate good ductility of the $Fe_{54}C_{18}Cr_{16}Mo_{12}$ BMG.

The temperature, at which the discontinuity of $Fe_{54}C_{18}Cr_{16}Mo_{12}$ BMG enthalpy-temperature profile during temperature elevation appears, is used to indicate the melting point of about 1310 K. The self-diffusion coefficients of $Fe_{54}C_{18}Cr_{16}Mo_{12}$ at temperatures near the melting point were calculated by the Einstein equation on the basis of the slopes of the MSD profiles at the long-time limit. On the basis of diffusion coefficients at different temperatures, the diffusion barriers of $Fe_{54}Cr_{16}Mo_{12}C_{18}$ can be determined by the Arrhenius equation. The diffusion barriers of total, Fe, Cr, Mo, C are 31.88, 24.68, 35.26, 22.50 and 31.79 KJ/mol, respectively. The diffusion barriers of Fe and Cr atoms are relatively lower, indicating Fe and Cr atoms more easily diffuse with the increasing temperature.

Reference:

[1] W. Klement, R. H. Willens, and P. Duwez, "Non-Crystalline Stucture In Solidified Gold-Silicon Alloys," *Nature*, *187*, 869-870, **1960**.

[2] A. Inoue, "High-Strength Bulk Amorphous Alloys with Low Critical Cooling Rates," *Materials Transactions Jim*, *36*, 866-875, **1995**.

[3] J. Q. Wang, J. Y. Qin, X. N. Gu, Y. F. Zheng, and H. Y. Bai, "Bulk Metallic Glasses Based on Ytterbium and Calcium," *Journal of Non-Crystalline Solids*, *3357*, 1232-1234, **2011**.

[4] Q. K. Jiang, G. Q. Zhang, L. Yang, X. D. Wang, K. Saksl, H. Franz, R. Wunderlich, H. Fecht, and J. Z. Jiang, "La-based Bulk Metallic Glasses with Critical Diameter up to 30 mm," *Acta Materialia*, *55*, 4409-4418, **2007**.

[5] Jianfeng Wang, Ran Li, Nengbin Hua, and Tao Zhang, " Co-based Ternary Bulk Metallic Glasses with Ultrahigh Strength and Plasticity," *Journal of Materials Research*, *26*, 2072, **2011**.

[6] Z. Q. Liu and Z. F. Zhang, " Strengthening and Toughening Metallic Glasses: The Elastic Perspectives and Opportunities," *Journal of Applied Physics*, *115*, 163505, **2014**.

[7] W. L. Johnson," Bulk Glass-Forming Metallic Alloys: Science and Technology," *Mrs Bull.*, *24*, 42-56, **1999**.

[8] A. Inoue, " Stabilization of Metallic Supercooled Liquid and Bulk Amorphous Alloys," *Acta Mater.*, *48*, 279-306, **2000**.

[9] J. J. Oak, D. V. Louzguine-Luzgin, and A. Inoue, " Fabrication of Ni-free Ti-based Bulk Metallic Glassy Alloy Having Potential for Application as Biomaterial, and Investigation of its Mechanical Properties, Corrosion, and Crystallization Behavior," *Journal of Materials Research*, *22*, 1346-1353, **2007**.

[10] H. F. Li, Y. F. Zheng, F. Xu, and J. Z. Jiang, " In Vitro Investigation of Novel Ni Free Zr-based Bulk Metallic Glasses as Potential Biomaterials," *Materials Letters*, *75*, 74-76, **2012**.

[11] X. N. Gu, N. Li, Y. F. Zheng, and L. Q. Ruan, " In Vitro Degradation Performance and Biological Response of a Mg-Zn-Zr Alloy," *Materials Science and Engineering B-Advanced Functional Solid-State Materials*, *176*, 1778-1784, **2011**.

[12] Mingxiao Zhang, Anding Wang, and Baolong Shen, "Enhancement of Glass-forming Ability of Fe-based Bulk Metallic Glasses with High Saturation Magnetic Flux Density," *AIP Advances, 2,* 022169*,* **2012**.

[13] Ryusuke Hasegawa, "Applications of Amorphous Magnetic Alloys in Electronic Devices," *Journal of Non-Crystalline Solids, 287,* 405-412*,* **2001**.

[14] Y.B. Wang, H.F. Li, Y. Cheng, S.C. Wei, Y.F. Zheng, "Corrosion Performances of a Nickel-free Fe-based Bulk Metallic Glass in Simulated Body Fuids," *Electrochemistry Communications, 11,* 2187–2190, **2009**.

[15] H. Zohdi, H.R. Shahverdi, S.M.M. Hadavi, "Effect of Nb Addition on Corrosion Behavior of Fe-based Metallic Glasses in Ringer's Solution for Biomedical Applications," *Electrochemistry Communications, 13,* 840-843, **2011**.

[16] C. Zhang, K.C. Chan, Y. Wu, L. Liu, " Pitting Initiation in Fe-based Amorphous Coatings," *Acta Materialia, 60,* 4152–4159, **2012**.

[17] M. Niinomi and M. Nakai, "Titanium-Based Biomaterials for Preventing Stress Shielding between Implant Devices and Bone," *International Journal of Biomaterials*, *2011*, 1-10, **2011**.

[18] W. Pilarczyk, R. Nowosielski, A. Januszka, "Structure And Properties of Fe-Cr-Mo-C Bulk Metallic Glasses Obtained by Die Casting Method, " *Journal of Achievements in Materials and Manufacturing Engineering*, *42*, 81-87, **2010**..

[19] X. J. Han and H. Teichler, "Liquid-to-glass Transition in Bulk Glass-forming $Cu_{60}Ti_{20}Zr_{20}$ Alloy by Molecular Dynamics Simulations," *Physical Review E, 75*, 061501, **2007**.

[20] S. W. Kao, C. C. Huang, and T. S. Chin, "Simulation of Reduced Glass Transition Temperature of Cu-Zr Alloys by Molecular Dynamics," *Journal of Applied Physics, 105*, 064913, **2009**.

[21] G. Grochola, S. P. Russo, and I. K. Snook, "On Fitting A Gold Embedded Atom Method Potential Using the Force Matching Method," *The Journal of Chemical Physics, 123*, 204719, **2005**.

[22] J. D. Honeycutt and H. C. Andersen, "Molecular Dynamics Study of Melting and Freezing of Small Lennard-Jones Clusters," *Journal of Physical Chemistry, 91*, 4950-4963, **1987**.

[23] B.-J. Lee, M.I. Baskes, Second Nearest-Neighbor Modified Embedded-Atom Method Potential, *Phys. Rev. B*, *62*, 8564–8567, **2000**.

[24] B.-J. Lee, M.I. Baskes, H. Kim, Y.K. Cho, Second Nearest-Neighbor Modified Embedded Atom Method Potentials for bcc Transition Metals, *Phys. Rev. B* , *64*, 184102, **2001**.

[25] F. Ercolessi and J. B. Adams, "Interatomic Potentials from 1st-Principles Calculations - the Force-Matching Method," *Europhysics Letters, 26*, 583-588, **1994**.

[26] D. J. Wales and J. P. K. Doye, "Global Optimization by Basin-hopping and the

Lowest Energy Structures of Lennard-Jones Clusters Containing up to 110 atoms," *Journal of Physical Chemistry A, 101*, 5111-5116, **1997**.

[27] S. Plimpton, " Fast Parallel Algorithms for Short-range Molecular Dynamics," *Journal of computational physics, 117*, 1-19, **1995**.

[28] N. Miyazaki and Y. Shiozaki, " Calculation of Mechanical Properties of Solids Using Molecular Dynamics Method," *Jsme International Journal Series a-Mechanics and Material Engineering, 39*, 606-612, **1996**.

[29] G. S. Pawley, " Unit-Cell Refinement from Powder Diffraction Scans," *Journal of Applied Crystallography, 14*, 357-361, **1981**.

[30] H. M. Rietveld, " A Profile Refinement Method for Nuclear and Magnetic Structures," *Journal of Applied Crystallography, 2*, 65-71, **1969**.

[31] J. E. Post and D. L. Bish, " Rietveld Refinement of Crystal-Structures Using Powder X-Ray Diffraction Data," *Reviews in Mineralogy, 20*, 277-308, **1989**.

[32] Materials Studio release 7.0, Accelrys Software Inc., San Diego, USA , **2013**.

[33] Y. C. Lo, J. C. Huang, S. P. Ju, and X. H. Du, "Atomic structure evolution of Zr-Ni during severe deformation by HA pair analysis," *Physical Review B, 76*, **2007**.

[34] V. Wessels, A. K. Gangopadhyay, K. K. Sahu, R. W. Hyers, S. M. Canepari, J. R. Rogers, M. J. Kramer,A. I. Goldman, D. Robinson, J. W. Lee, J. R. Morris, and K. F. Kelton, " Rapid Chemical and Topological Ordering in Supercooled Liquid $Cu_{46}Zr_{54}$," *Physical Review B, 83,* 094116, **2011**.

[35] Hui-Lung Chen, Shin-Pon Ju, Tsang-Yu Wu, Shih-Hao Liu and Hsin-Tsung Chen," Investigation of the Mechanical Properties and Local Structural Evolution of $Ti_{60}Zr_{10}Ta_{15}Si_{15}$ Bulk Metallic Glass during Tensile Deformation: A Molecular Dynamics Study," *RSC Advances., 5*, 55383, **2015**.

[36] Shin-Pon Ju, Tsang-Yu Wu, and Shih-Hao Liu," Mechanical and Dynamical Behaviors of ZrSi and $ZrSi_2$ Bulk Metallic Glasses: A Molecular Dynamics Study," *Journal of Applied Physics, 117,* 105103, **2015**.

[37] Shin-Pon Ju, Hsin-Hong Huang, Tsang-Yu Wu, "Investigation of the Local Structural Rearrangement of $Mg_{67}Zn_{28}Ca_5$ Bulk Metallic Glasses during Tensile Deformation: A Molecular Dynamics Study," *Computational Materials Science,* 96 , 56–62, **2015**.

[38] R. N. Singh and F. Sommer, "Segregation and Immiscibility in Liquid Binary Alloys," *Reports on Progress in Physics, 60*, 57-150, **1997**.

[39] S.F. Guo,L. Liu,N. Li and Y. Li,"Fe-based Bulk Metallic Glass Matrix Composite with Large Plasticity," *Scripta Materialia*, *62*, 329–332, **2010**.

[40] S. F. Guo,J. L. Qiu,P. Yu,S. H. Xie,and W. Chen," Fe-based Bulk Metallic Glasses: Brittle or Ductile?," *Applied Physics Letters , 105,* 161901 , **2014.**

[41] X. D. Wang, H. B. Lou, J. Bednarcik, H. Franz, H. W. Sheng, Q. P. Cao, and J. Z. Jiang, "Structural Evolution in Bulk Metallic Glass under High-Temperature Tension," *Applied Physics Letters, 102*, 051909, **2013**.

[42] F. Shimizu, S. Ogata, and J. Li, "Theory of shear banding in metallic glasses and molecular dynamics calculations," *Materials Transactions, 48*, 2923-2927, **2007**.

[43] J. T. Wang, P. D. Hodgson, J. D. Zhang, W. Y. Yan, and C. H. Yang, "Effects of Pores on Shear Bands in Metallic Glasses: A Molecular Dynamics Study," *Computational Materials Science, 50*, 211-217, **2010**.

[44] K. Albe, Y. Ritter, and D. Şopu, "Enhancing the Plasticity of Metallic Glasses: Shear Band Formation, Nanocomposites and Nanoglasses Investigated by Molecular Dynamics Simulations," *Mechanics of Materials, 67*, 94-103, **2013**.

[45] J.-J. Oak and A. Inoue, "Attempt to Develop Ti-based Amorphous Alloys for Biomaterials," *Materials Science and Engineering: A, 449*, 220-224, **2007**.

[46] J. S. C. Jang, S. R. Jian, C. F. Chang, L. J. Chang, Y. C. Huang, T. H. Li, J. C. Huang, and C. T. Liu, "Thermal and Mechanical Properties of the $Zr_{53}Cu_{30}Ni_9Al_8$ based Bulk Metallic Glass Microalloyed with Silicon," *Journal of Alloys and Compounds, 478*, 215-219, **2009**.

[47] Yue Qi, Tahir Cagın, Yoshitaka Kimura, and William A. Goddard III, "Molecular-dynamics simulations of glass formation and crystallization in binary liquid metals: Cu-Ag and Cu-Ni," *Physical Review B, 59*, 3527-3533, **1999**.

[48] M. Meunier, " Diffusion Coefficients of Small Gas Molecules in Amorphous Cis-1,4-polybutadiene Estimated by Molecular Dynamics Simulations," *J. Chem. Phys., 123,* 134906, 2005.

[49] Soumitra Roy, Aloke Paul, " Growth of Hafnium and Zirconium Silicides by Reactive Diffusion," *Mater. Chem. Phys., 143*, 1309-1314, **2014**.

[50] H. L. Peng, M. Z. Li and W. H. Wang," Structural Signature of Plastic Deformation in Metallic Glasses," *Phys. Rev. Lett*., *106* , 135503, **2011**.

Table I. Average coordination numbers (CNs) for Fe, C, Cr and Mo atoms and each pair in $Fe_{54}C_{18}Cr_{16}Mo_{12}$ BMG.

$Fe_{54}C_{18}Cr_{16}Mo_{12}$ BMG					
Type	***Fe-Fe***	***Fe-Cr***	***Fe-Mo***	***Fe-C***	***Fe_Total***
N_{ij}	5.77	2.16	1.48	2.29	11.70
Type	***Cr-Fe***	***Cr-Cr***	***Cr-Mo***	***Cr-C***	***Cr_Total***
N_{ij}	6.54	1.97	1.69	2.28	12.48
Type	***Mo-Fe***	***Mo-Cr***	***Mo-Mo***	***Mo-C***	***Mo_Total***
N_{ij}	5.99	2.32	1.45	2.40	12.16
Type	***C-Fe***	***C-Cr***	***C-Mo***	***C-C***	***C_Total***
N_{ij}	6.20	2.05	1.56	2.13	11.94

Table II. CSRO parameters (α_{ij}) for all atomic pairs of $Fe_{54}C_{18}Cr_{16}Mo_{12}$ BMG.

$Fe_{54}C_{18}Cr_{16}Mo_{12}$ BMG				
Type	***Fe-Fe***	***Fe-Cr***	***Fe-Mo***	***Fe-C***
α_{ij}	0.086	-0.155	-0.54	-0.085
Type	***Cr-Fe***	***Cr-Cr***	***Cr-Mo***	***Cr-C***
α_{ij}	0.030	0.013	-0.129	-0.016
Type	***Mo-Fe***	***Mo-Cr***	***Mo-Mo***	***Mo-C***
α_{ij}	0.111	-0.163	0.032	-0.067
Type	***C-Fe***	***C-Cr***	***C-Mo***	***C-C***
α_{ij}	0.039	-0.075	-0.088	0.007

Table III. The estimated pre-exponential factor (D_0) and activation energy (Q) of $Fe_{54}C_{18}Cr_{16}Mo_{12}$ BMG.

Temperature interval	Type	D_0 (m^2 s^{-1})	Q (kJ mol^{-1})
800-1400 K	**Total**	2.72e-10	31.88
	Fe	1.13e-10	24.68
	C	4.28e-10	35.26
	Cr	7.70e-11	22.50
	Mo	2.03e-10	31.79

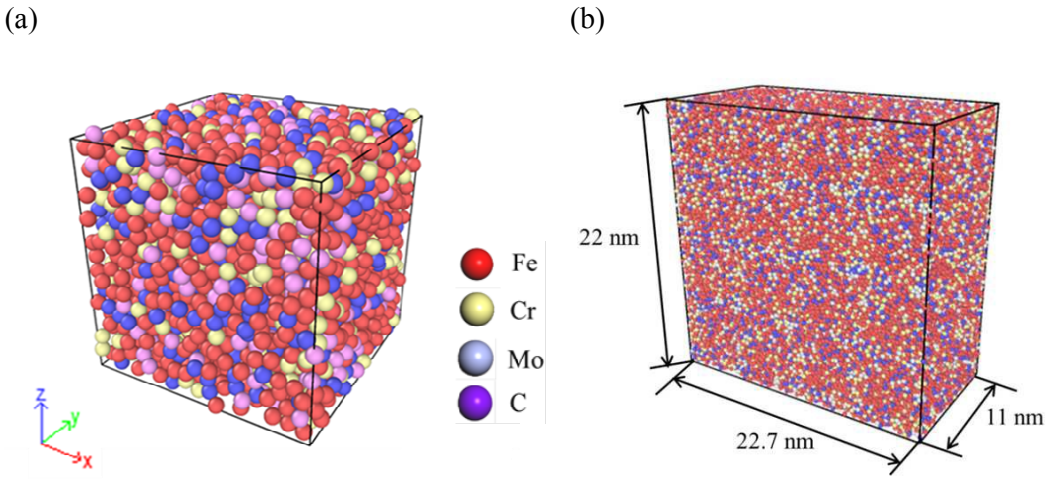

Fig. 1. Structures of (a) unit cell and (b) tensile test model for $Fe_{54}C_{18}Cr_{16}Mo_{12}$ BMG.

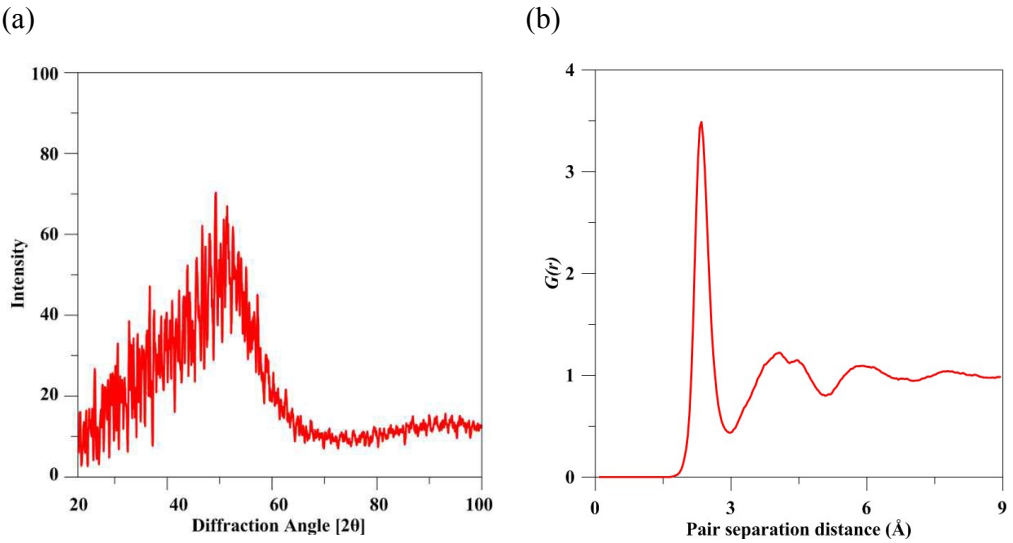

Fig. 2. (a) Simulated XRD pattern and (b) RDF profile for the $Fe_{54}C_{18}Cr_{16}Mo_{12}$ BMG.

(a)

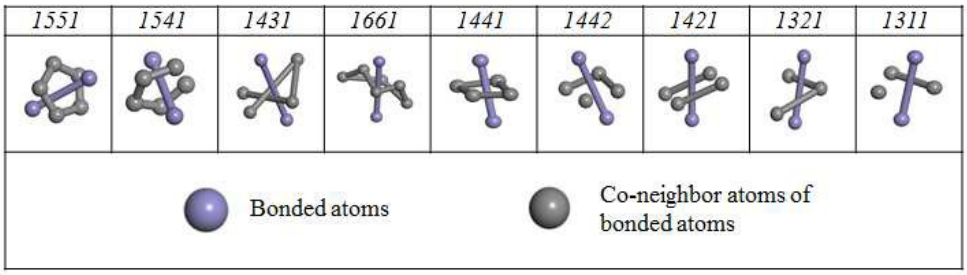

(b)

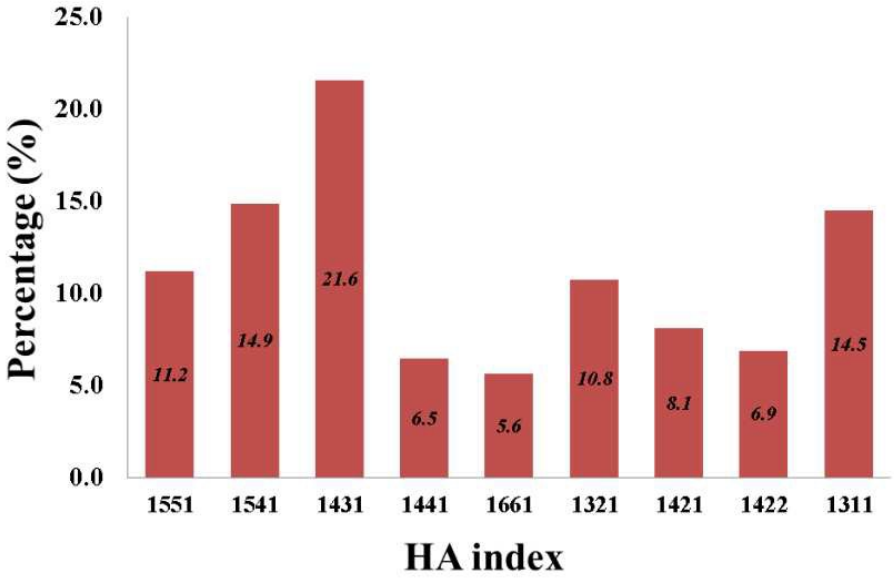

Fig. 3. (a) Schematic diagrams corresponding to several characteristic HA indexes; (b) HA index numbers for $Fe_{54}C_{18}Cr_{16}Mo_{12}$ BMG.

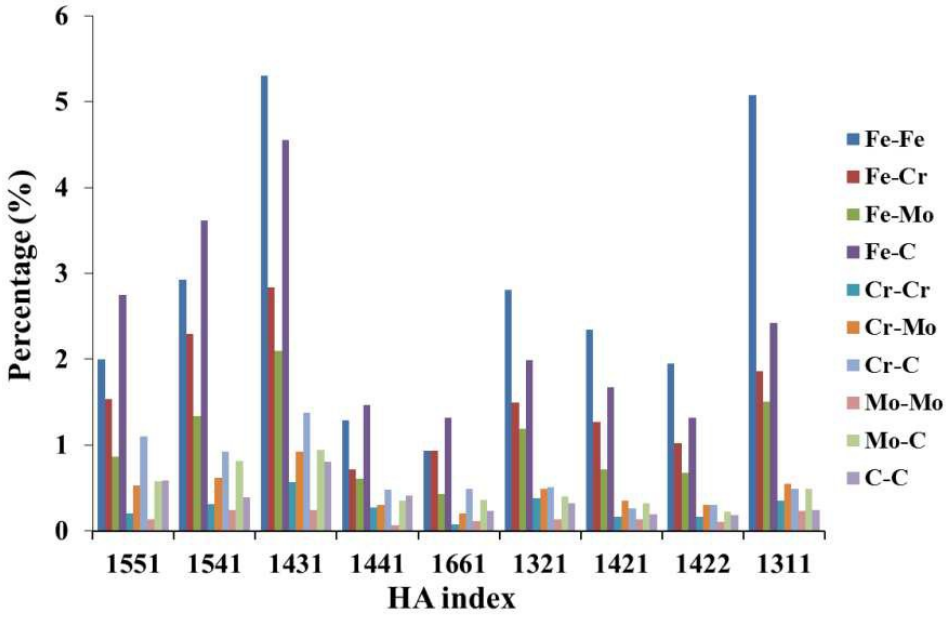

Fig. 4. The HA indexes for different pairs of the $Fe_{54}C_{18}Cr_{16}Mo_{12}$ BMG.

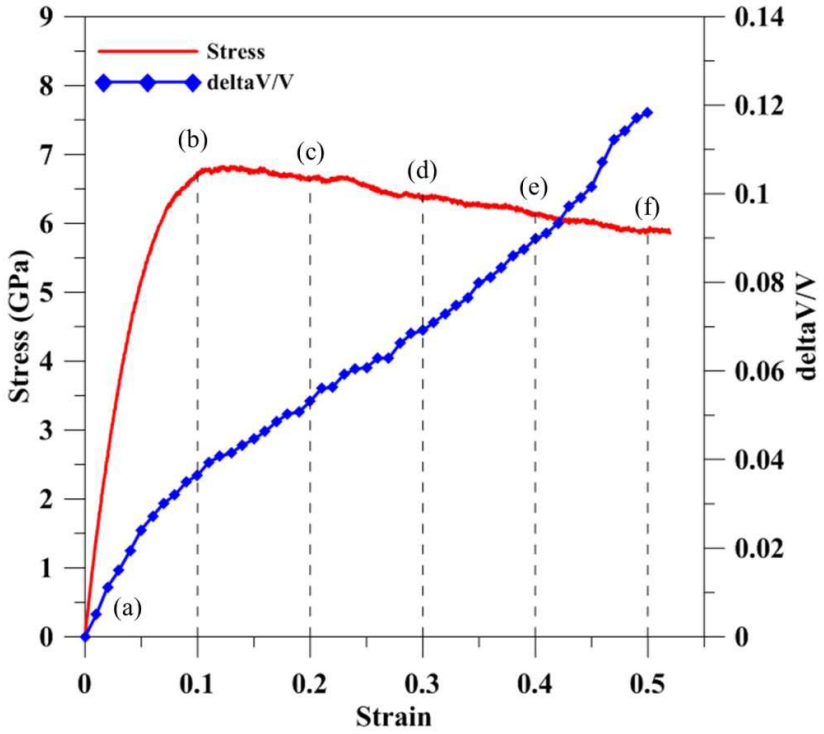

Fig. 5. The stress–strain curve and ΔV/V for $Fe_{54}C_{18}Cr_{16}Mo_{12}$ BMG.

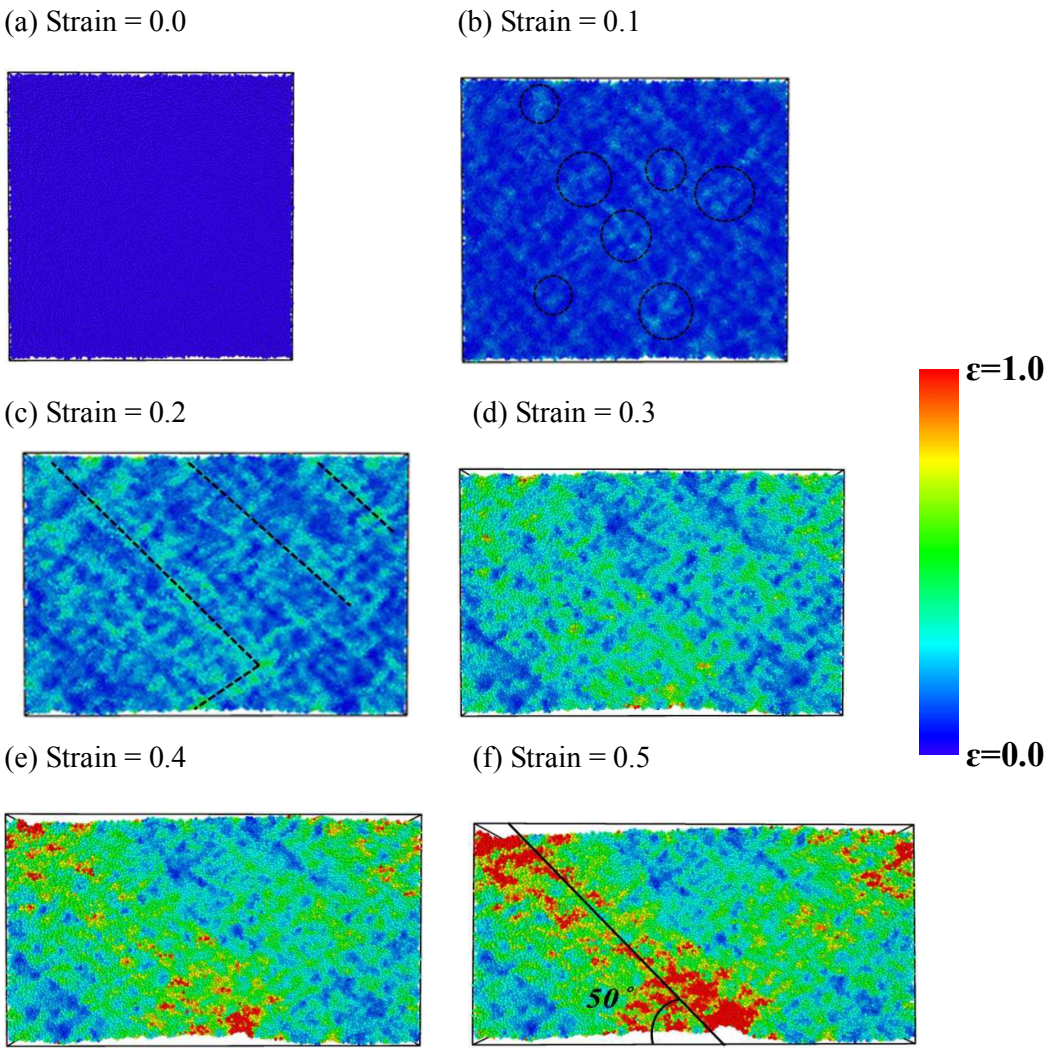

Fig. 6. The distribution of atomic local shear strain.

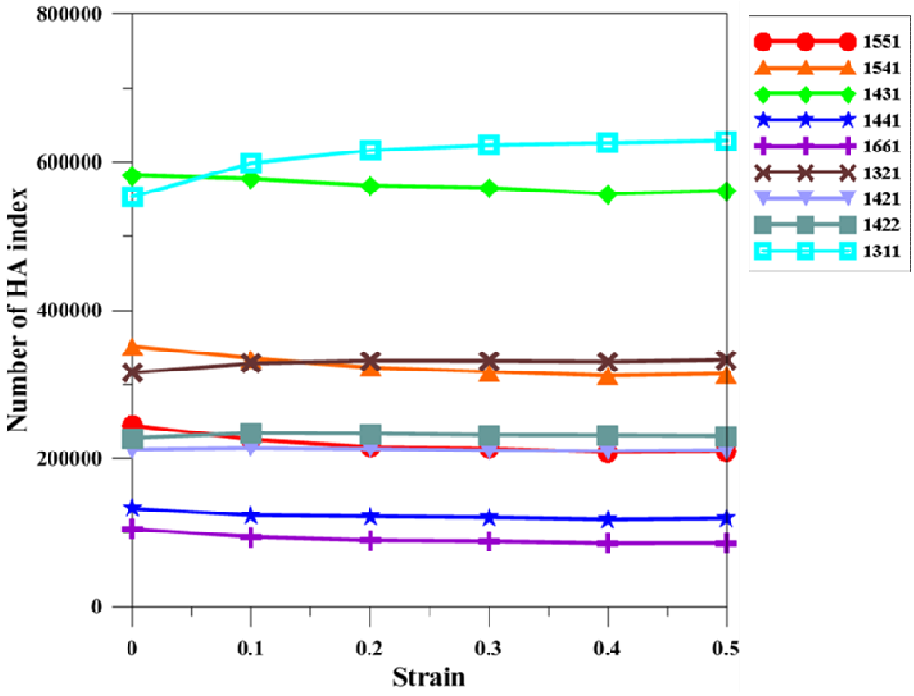

Fig. 7. The HA indexes at different strains for $Fe_{54}C_{18}Cr_{16}Mo_{12}$ BMG.

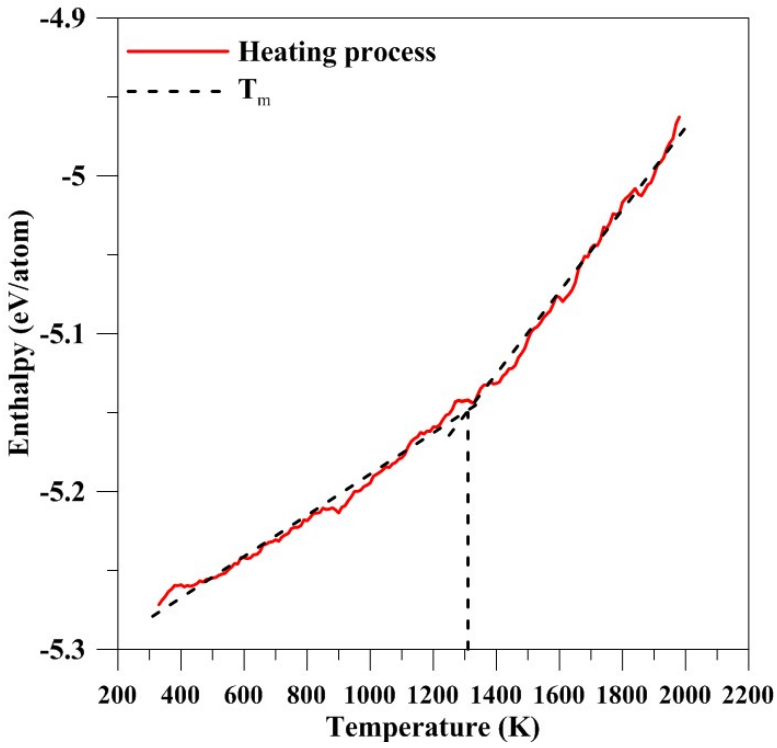

Fig. 8 Average enthalpy versus temperature for $Fe_{54}C_{18}Cr_{16}Mo_{12}$ BMG.

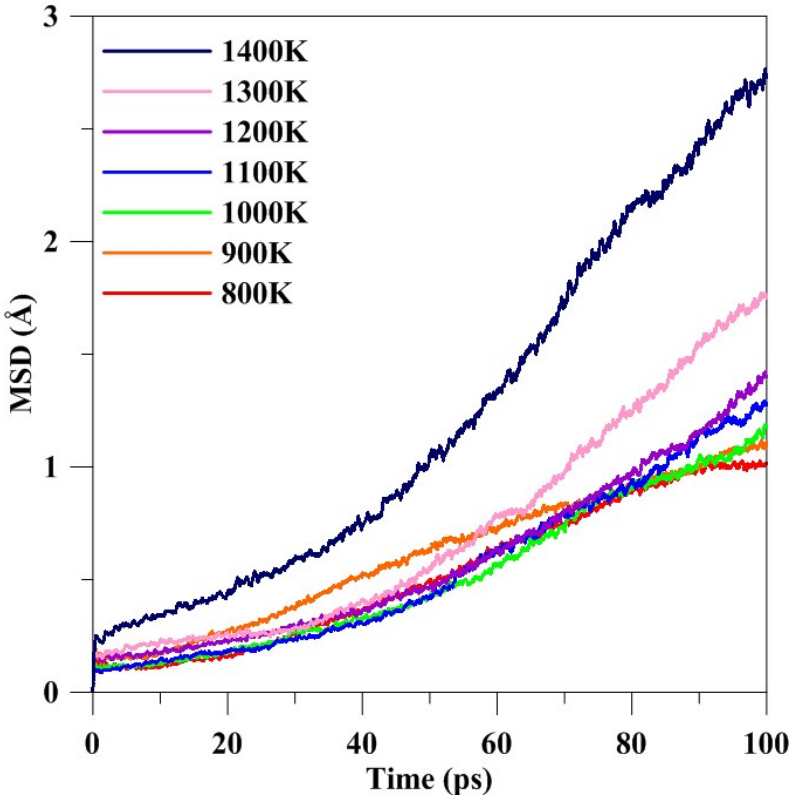

Fig. 9 The mean-square displacement plots (MSD) of $Fe_{54}C_{18}Cr_{16}Mo_{12}$ BMG.

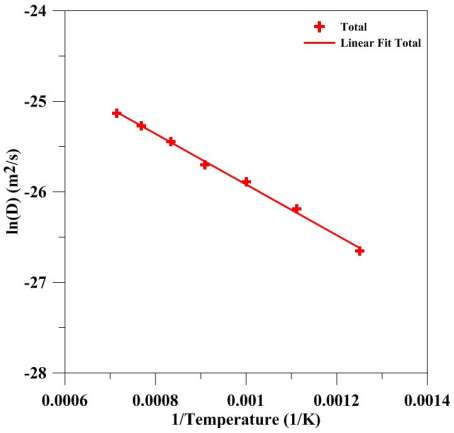

(a)

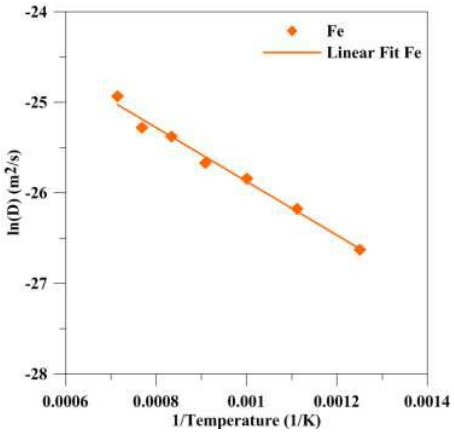

(b)

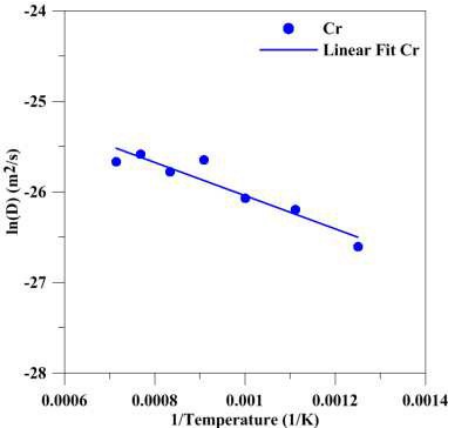

(c)

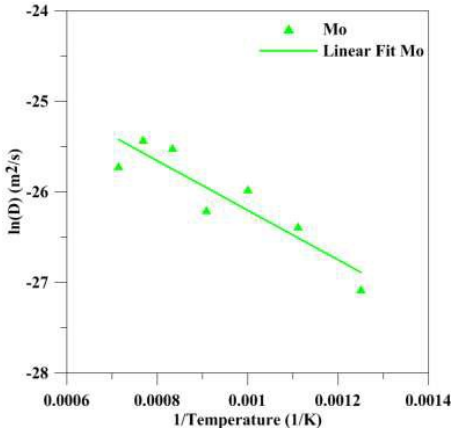

(d)

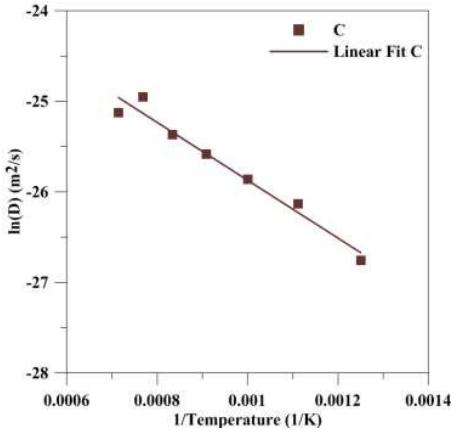

(e)

Fig. 10 Diffusion coefficient for $Fe_{54}C_{18}Cr_{16}Mo_{12}$ BMG: (a) total, (b) Fe, (c) Cr, (d) Mo, and (e) C atoms

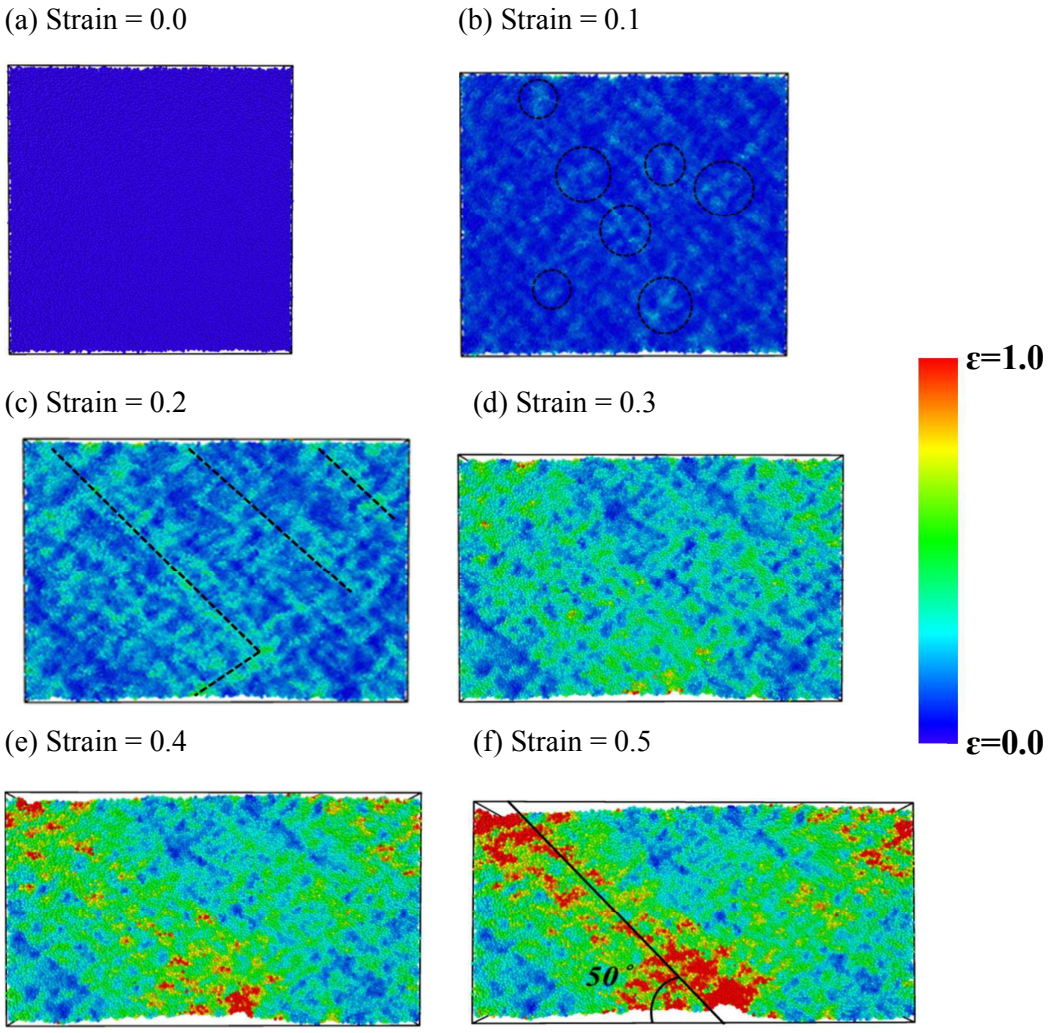

The mechanical and thermal properties of $Fe_{54}C_{18}Cr_{16}Mo_{12}$ bulk metallic glasses (BMGs) were investigated by the molecular dynamics simulation with the 2NN modified embedded-atom method (MEAM) potential. Local strain distribution was used to analyze the deformation mechanism, and results show that a shear band develops homogeneously with the tensile fracture angle (θ_T) at about 50 degrees, in agreement with experimental results $45° < \theta_T < 90°$.